

Histo-Cytometry: A Method for Highly Multiplex Quantitative Tissue Imaging Analysis Applied to Dendritic Cell Subset Microanatomy in Lymph Nodes

Michael Y. Gerner,^{1,*} Wolfgang Kastentmuller,¹ Ina Ifrim,¹ Juraj Kabat,² and Ronald N. Germain^{1,*}

¹Lymphocyte Biology Section, Laboratory of Systems Biology

²Biological Imaging Section, Research Technology Branch

National Institute of Allergy and Infectious Diseases, National Institutes of Health, Bethesda, MD 20892, USA

*Correspondence: gernermy@niaid.nih.gov (M.Y.G.), rgermain@nih.gov (R.N.G.)

<http://dx.doi.org/10.1016/j.immuni.2012.07.011>

SUMMARY

Flow cytometry allows highly quantitative analysis of complex dissociated populations at the cost of neglecting their tissue localization. In contrast, conventional microscopy methods provide spatial information, but visualization and quantification of cellular subsets defined by complex phenotypic marker combinations is challenging. Here, we describe an analytical microscopy method, “histo-cytometry,” for visualizing and quantifying phenotypically complex cell populations directly in tissue sections. This technology is based on multiplexed antibody staining, tiled high-resolution confocal microscopy, voxel gating, volumetric cell rendering, and quantitative analysis. We have tested this technology on various innate and adaptive immune populations in murine lymph nodes (LNs) and were able to identify complex cellular subsets and phenotypes, achieving quantitatively similar results to flow cytometry, while also gathering cellular positional information. Here, we employ histo-cytometry to describe the spatial segregation of resident and migratory dendritic cell subsets into specialized microanatomical domains, suggesting an unexpected LN demarcation into discrete functional compartments.

INTRODUCTION

The innate and adaptive immune systems contain an exceptional diversity of hematopoietic cell subpopulations (Germain, 2004), whose fine-grained identification comes from use of monoclonal antibodies (Köhler and Milstein, 1975) for fluorescence-based flow cytometry with as many as 17 parameters (Perfetto et al., 2004) or for a new mass spectrometry-based method that permits >40 features to be studied at once (Bendall et al., 2011; Newell et al., 2012). Cell types initially believed to represent a single lineage are now understood to comprise many distinct subsets with divergent functions. At the same time, optical tissue imaging has revealed the specialized anatomical localization of a few of these cellular subsets in the steady state or after stimu-

lation (Kastentmuller et al., 2012), for example, the repositioning of activated B cells at the T-B border (Ansel et al., 1999; Garside et al., 1998; Reif et al., 2002). This heterogeneity and the crucial role played by tissue anatomy and cellular positioning in immunity raise a key issue. Microscopic imaging typically identifies cells by one or a very few markers, in striking contrast to flow cytometric methods. This sparse analysis precludes relating the spatial insights obtainable from optical imaging with the dense phenotypic data derived from flow analysis. Yet only a combination of the two can provide optimal assessments of the immune system in health and disease.

Dendritic cells (DCs) are a cell type for which a method that can combine these two technologies would be of particular value (Chow et al., 2011). DCs are critically involved in detecting and processing information from invading pathogens and regulating the activation and differentiation of T cells (Heath and Carbone, 2009). DCs, often characterized just by coexpression of major histocompatibility complex class II (MHC-II) molecules and CD11c, are in reality a highly heterogeneous population with variable expression of lectins, Toll-like receptors, inflammatory cytokines, and costimulatory molecules. Distinguishable DC subpopulations play specialized roles in sensing various infections and differentially stimulate CD8⁺ and CD4⁺ T cells (Edwards et al., 2003; Heath and Carbone, 2009; Helft et al., 2010; Igyártó et al., 2011; Sancho et al., 2009; Shortman and Heath, 2010). As a prime example of subset complexity within tissues, murine skin draining lymph nodes (dLNs) typically contain conventional CD11c^{hi}MHC-II^{int} lymphoid-tissue resident DCs (composed of CD8⁺ and CD11b⁺ subsets), CD11c^{int}MHC-II^{hi} peripheral tissue-derived migratory DCs (composed of CD207⁺CD103⁺ dermal DC (dDCs), CD11b⁺CD207⁺CD103⁺ dDC, and CD207⁺CD103⁺ Langerhans cells [LCs]), and B220⁺ plasmacytoid DCs (Heath and Carbone, 2009; Helft et al., 2010; Villadangos and Schnorrer, 2007).

Given that DC subset markers are not exclusively expressed by one or another subpopulation, image-based analysis of subset-specific localization differences has been challenging. Nevertheless, after fluorophore skin painting of Langerin (CD207) reporter animals, migratory CD207⁺ dDC and CD207⁺ DC (a combination of LC and CD103⁺ dDC) were found to localize to discrete areas of dLNs (Kissenpfennig et al., 2005). Most other reports visualizing lymphoid tissue-resident DC subsets have focused on the spleen, with its greatly reduced DC heterogeneity. Such studies have documented localization

of DC subpopulations to discrete microcompartments (Dudziak et al., 2007; Idoyaga et al., 2009; Qiu et al., 2009) and location-specific differences in antigen (Ag) sampling, infectious spread, and cytokine production (Edelson et al., 2011; Qiu et al., 2009; Rothfuchs et al., 2009).

These findings highlight the need for robust identification, visualization, and quantification of complex cellular populations directly in tissues. Such methodology requires staining with and visualization of multiple phenotype-specific antibodies, together with analysis of large tissue areas for cells possessing the relevant marker combinations. Although commercially available microscopes can discriminate numerous fluorophores and image large areas at high resolution (Conchello and Lichtman, 2005; Garini et al., 2006), there are virtually no reports examining cell subpopulations identified by highly multiplex marker expression directly in situ.

By combining multiparameter 3D confocal imaging, spillover and deconvolution correction, identification and 3D reconstruction of specific cells of interest (COI), and graphical data display, we have developed an analytical pipeline, “histo-cytometry,” that allows visualization, quantification, and positional analysis directly in tissue sections of diverse cell populations characterized by multiple markers. Here, we describe the method, validating the approach by analyzing various adaptive immune cell subsets in LN sections and by tracking phenotypic changes occurring in Ag-specific T cells upon activation. We also utilize histo-cytometry to examine the spatial distribution of highly heterogeneous conventional DC subsets in unperturbed LNs. We report anatomical segregation of distinct resident and migratory DC subsets, suggesting a highly regulated, fine-grained organization of LNs into functionally discrete spatial microdomains whose existence has important implications for understanding how polarized immune responses develop and for designing vaccine strategies in which delivery of material to the right DC subset is crucial.

RESULTS

Histo-Cytometry: Methodology

To gain positional and quantitative information on complex cellular subsets and phenotypes (defined by multiple markers) directly in tissue sections, we have devised a general histo-cytometry workflow (Figure 1). First, LN cross-sections were stained with large panels of phenotypically appropriate fluorescently-labeled antibodies, six to eight colors at present, although in principle the method can be applied to more colors (Figure 1, step 1). Because of the densely packed nature of tissues, high-resolution imaging and accurate signal 3D allocation is needed for optimal signal to cell assignment (Scriven et al., 2008). However, a practical balance must be achieved between the highest-possible image resolution, the overall imaging volume, and imaging duration. Limitations to super-resolution microscopy in this context make conventional diffraction-limited confocal microscopy the most practical choice (Hell, 2009). With this latter technology, accurate signal allocation of multiple different fluorophores in all three axes (x, y, z) can be achieved with high numerical aperture (NA) objectives. In addition, deconvolution algorithms that mathematically reverse optical distortions can be applied after initial data acquisition

to improve image quality (Conchello and Lichtman, 2005). Therefore in our processing pipeline, the stained tissues were imaged at high optical resolution with conventional tiling confocal microscopes capable of discriminating multiple spectrally-distinct fluorophores (Figure 1, step 1), with the optical distortions minimized by postimaging deconvolution (Figure 1, step 2).

As in flow cytometry, highly multiplex staining that uses fluorophores with overlapping emission spectra generates substantial spillover artifacts and thus requires compensation correction (Conchello and Lichtman, 2005). Although some microscopy systems can collect hyperspectral data and remove fluorophore crosstalk through spectral unmixing, it is more practical to collect single-stain control images and calculate the relative spillover of each fluorophore into the other detectors. We mathematically applied simple compensation correction algorithms to every imaged voxel after data acquisition in a manner akin to flow cytometry (Roederer, 2002) (Figure 1, step 3, and Figure S1A available online).

Because of the lack of molecular level resolution, diffraction-limited confocal imaging does not spatially separate neighboring fluorescent molecules, instead colocalizing them to the same voxel (volumetric pixel). This makes correct signal to cell allocation potentially problematic in densely packed tissues (Scriven et al., 2008). However, such photon colocalization can also be used for software-based identification of voxels displaying specific combinations of markers. Thus, by selecting (“gating”) voxels positive for fluorescent signals from COI-specific antibodies and negative for irrelevant or inappropriate cell markers, we could identify discrete image regions corresponding to COI and not to contaminating noise or irrelevant cells (Figure 1, step 4), a process highly similar to flow cytometric Boolean gating and the use of “dump” channels for exclusion of irrelevant cell populations (Roederer, 2002). This was accomplished by creation of a new COI-specific binary channel based on the selected fluorescence thresholds, identified by visually guided semiautomated thresholding (Figures S1B and S1C). The new COI binary channel was then used for masking all other relevant parameters, thus effectively reducing the image complexity only to the COI and allowing for qualitative visualization of distinct cellular subsets (Figure 1, step 5, and Figure S1D).

Finally, to achieve flow cytometry-like cellular phenotypic profiling and quantification, we created 3D volumetric surface objects corresponding to individual cells by utilizing the semiautomatic surface rendering module in the Imaris imaging software (Figure 1, step 6). Surface segmentation algorithms can suffer from poor separation of very dense, phenotypically homogeneous cellular clusters, especially when visualizing surface markers. Nevertheless, for many important questions it is currently possible to analyze tissue sections for relatively nonclustered COI. In turn, COI-based surface objects have various quantitative information associated with them, including (x, y, z) position and average voxel fluorescence intensities for the imaged parameters. Through graphical plotting of these parameters, we achieved quantitative phenotypic subset analysis (akin to flow cytometry) with the added bonus of subset-specific positional characterization within the tissue (Figure 1, steps 7 and 8).

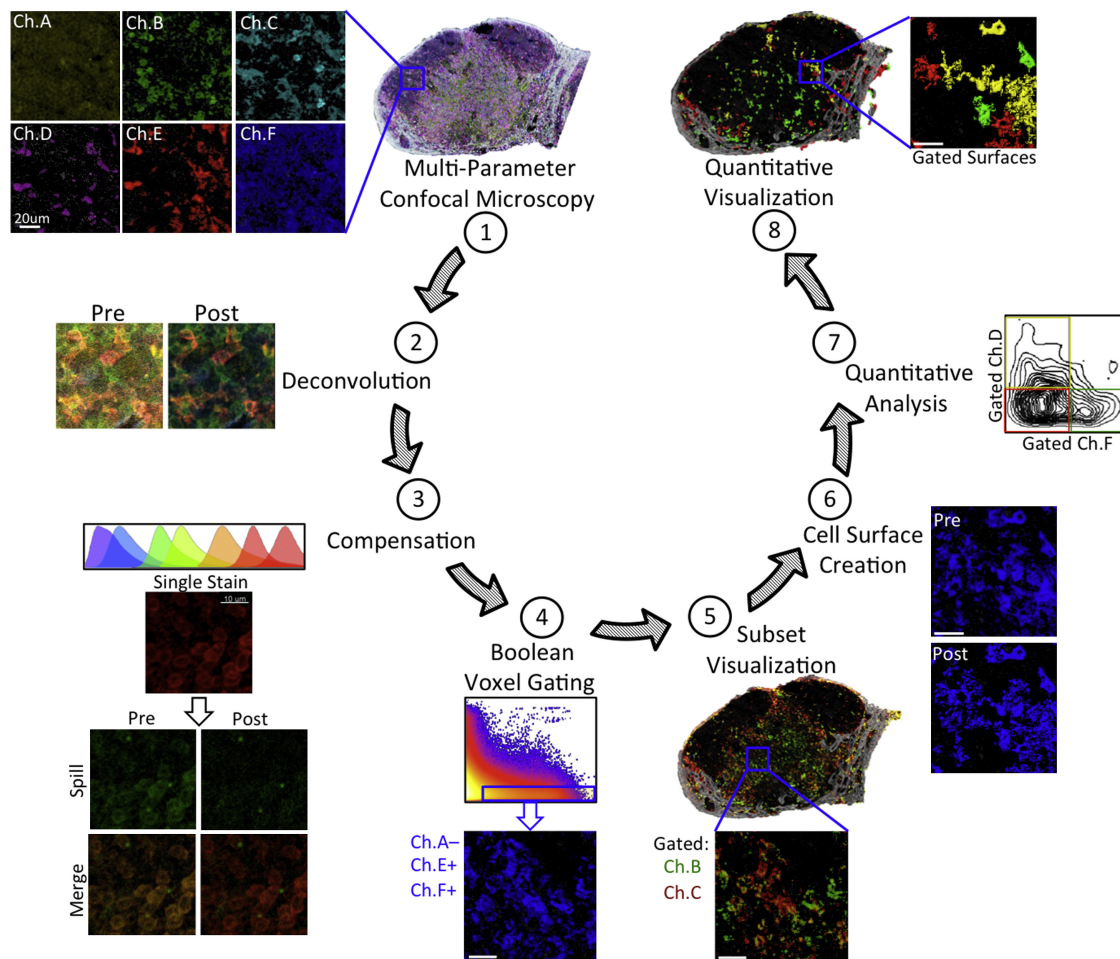


Figure 1. Histo-Cytometry Workflow Pipeline

Multiparameter confocal images of tissue sections are taken with a tiling confocal microscope (1). Images are then deconvolved (2) and compensated for fluorophore spillover (3). Voxels exhibiting specified combinations of signals in the original channels (above or below designated thresholds) are used for creating a new masking channel (4), which is then used to mask (gate) all other parameters of interest (5). 3D COI surfaces are constructed on the basis of the gated signal expressed by the COI through use of semiautomatic volumetric rendering and segmentation (6). COI surface statistics are exported for quantitative analysis and phenotypic gating (7), and the identified gate thresholds are used for quantitative visualization (8). Scale bars represent 20 µm, unless otherwise stated.

Basic Immune Subset Discrimination

We first tested the ability of this histo-cytometry method to accurately identify and quantify major immune subsets in sections from cell subpopulation-rich LNs. Bone marrow (BM) chimeric animals were constructed by transfer of 1:99, 5:95, or 10:90 mixtures of CD45.2⁺ BM and CD45.1⁺ donor BM into irradiated CD45.1⁺ recipients, and histo-cytometry was used for identifying different CD45.2⁺ cell subsets in cutaneous LN after reconstitution (Figure 2A). In this scenario, the CD45.2⁺ COI would be represented in all hematopoietic cellular lineages, with distinct populations reconstituting with slightly different frequencies in each chimeric animal. These cells would not be directly adjacent to one another, thus allowing for membrane-based segmentation, but they would still be surrounded by numerous irrelevant CD45.1⁺ cells and would be located in their usual microanatomical compartments. The quantitative data obtained from microscopic imaging were compared with flow

cytometric analysis of cells from dissociated contralateral LNs of the same animals (Figure 2A).

We stained the LN sections with a panel of antibodies for discriminating between the CD45.2⁺ and CD45.1⁺ cells and for identifying specific leukocyte subsets. We then imaged whole LN sections, deconvolved the data, and compensated for fluorophore spillover (Figure 2B and data not shown). To minimize signal contamination from closely apposed CD45.1⁺ irrelevant cells, we selectively gated on CD45.2⁺CD45.1⁻ voxels to create a new binary colocalization channel specifically representing only the CD45.2⁺ COI (Figure 2C). This channel was then used for masking other parameters of interest, thus allowing visualization of individual CD45.2⁺ cells belonging to one or another lymphoid lineage (Figure 2C). We next volumetrically rendered the gated CD45.2 signal, thus creating 3D surface objects representing the CD45.2⁺ COI, and exported the statistics for further analysis (Figure 2C). Plotting these data as 2D histograms

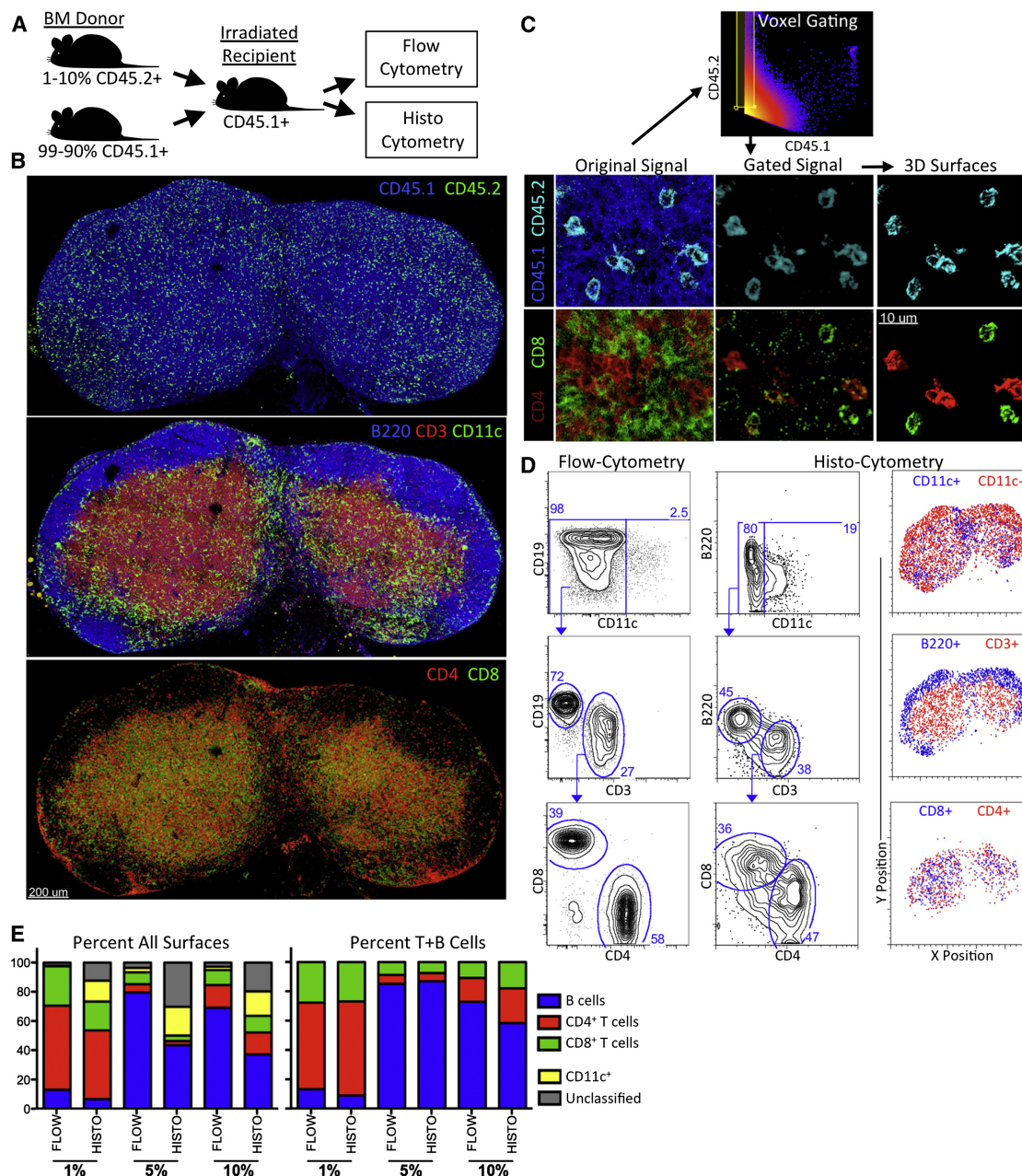


Figure 2. Basic Immune Subset Discrimination

Irradiated CD45.1⁺ recipients were injected with a 1:99, 5:95, or 10:90 mixture of CD45.2⁺ to CD45.1⁺ donor BM and were allowed to reconstitute for 6 weeks, after which contralateral inguinal LNs were taken for comparative analysis by flow cytometry and histo-cytometry (A). LN sections were stained with a panel of indicated antibodies and imaged (B). CD45.2⁺CD45.1⁻ voxels were used for creating a masking channel that was utilized to further gate all other imaged parameters, with the gated CD45.2 signal used for creating 3D surface renderings of CD45.2⁺ cells (C). Surface statistics were exported and plotted for identification of distinct immune subsets and compared to results obtained by flow cytometry (D). x and y positions of CD45.2⁺ surfaces were plotted for each subset (D). Relative frequencies of identified subsets in the 1%–10% chimeric animals, with (left) or without (right) inclusion of CD11c⁺ and unclassified events, were determined and compared to flow cytometry-based quantification (E). A representative of three independent imaging quantifications is shown.

revealed the capacity of the method to provide cellular subset discrimination of CD11c⁺ cells, B cells (B220⁺CD3⁻CD11c⁻), and CD4⁺ and CD8⁺ T cells (CD3⁺B220⁻CD11c⁻) with patterns that were similar to the data derived from flow cytometric analysis of dissociated cells (Figures 2D and 2C). Moreover, the x,y positional information of individual cell surfaces allowed us to

visualize the spatial distribution of gated subsets within the LN. We observed localization of computed B cell surfaces to structures corresponding to the B cell follicles, of CD4⁺ and CD8⁺ T cell surfaces to the T cell zone, and of CD11c⁺ surfaces to the paracortical T cell zone and with somewhat higher densities the interfollicular and lymphatic regions (Figure 2D).

Histo-cytometry-based cell positioning was thus consistent with the normal biological localization of these cell types (Figure 2B).

Quantitative subset discrimination also allowed comparisons to flow cytometric analysis of cells from the contra-lateral LN. CD45.2⁺ B cells, CD4⁺ T cells, and CD8⁺ T cells in the different chimeras showed a near 1:1 correspondence between flow cytometry and histo-cytometry methods, suggesting that histo-cytometry can also be used for quantitative analysis of cell subset composition, at least for cells of this simple morphology (Figure 2E). However, there were also clear differences between these analyses. Histo-cytometry yielded markedly higher percentages of CD11c⁺ cells relative to flow cytometry. Given that CD11c⁺ DC are cells of very high morphological complexity, the use of semiautomatic segmentation algorithms resulted in cellular oversegmentation of 6%–17% of CD11c⁺ events, depending on the particular image analyzed (data not shown), yielding multiple apparent cells from what is in reality a single cell. We therefore manually curated the cellular surfaces to exclude oversegmentation artifacts. Even with this adjustment, the frequency of CD11c⁺ cells identified via histo-cytometry greatly exceeded that derived from flow cytometry (Figure 2E). Because DCs tightly bind stromal elements of the LN and are difficult to extract even with standard tissue disruption methods (Vremec et al., 1992), these cells can be underrepresented in flow cytometric analysis of single-cell suspensions. The absence of extraction artifacts with histo-cytometry may therefore provide a more accurate and complete picture of DC frequency and location. On the other hand, a number of surfaces could not be clearly allocated to a distinct lineage, potentially because of decreased fluorescence separation in microscopy-based analyses as compared to flow cytometry or to noise contamination derived from spatially proximal cells (Figure 2E).

Besides analysis of spatially separated CD45.2⁺ cellular events, complete quantitative analysis of all constituent cells within an imaged tissue section is highly desirable. Membrane staining alone does not currently allow for segmentation of tightly juxtaposed cells with shared surface phenotype. However, cellular nuclei are relatively well separated spatially, and we found that it was possible to segment most cellular events in the imaged LN on the basis of nuclear staining (Figure S2A). Resting T and B lymphocytes have relatively small cytoplasmic volumes and the majority of the cellular membranes lie in close nuclear proximity. This provided sufficient signal overlap between membrane staining and the nuclear dye signal to allow nuclear surface-based cell subset gating and quantification (Figure S2B). By excluding poorly segmented events through volumetric and nuclear MFI gating, when looking at CD45.1⁺ and CD45.2⁺ events, we were able to identify all B cell, CD4⁺ and CD8⁺ T cell subpopulations within the imaged LNs despite dense cell packing. The cellular frequencies closely matched the membrane-based histo-cytometry data for CD45.2⁺ events and flow cytometry data for both CD45.1⁺ and CD45.2⁺ populations (Figures S2C and S2D). This specialized segmentation method relies on close juxtaposition of the plasma membrane with the nucleus, making it suitable strictly for quantitative analysis of resting lymphocytes and not for blasting or morphological complex cell populations.

Phenotypic Profiling of T cell Activation

We then examined histo-cytometry for its capacity to detect well-characterized stimulus-associated phenotypic changes in defined cellular subsets. Upon sensing cognate antigens during infection or immunization, CD8⁺ and CD4⁺ T cells undergo rapid activation and cellular proliferation, processes associated with changes in expression of distinct surface markers and cell cycle proteins (Smith-Garvin et al., 2009). We attempted to visualize these phenotypic changes in responding Ag-specific T cells directly in tissue sections and to determine the spatial distribution of T cell activation with respect to the location of cognate Ag within the LN. CD45.2⁺ OVA-specific T cell receptor (TCR) transgenic CD8⁺ (OT-I) and CD4⁺ (OT-II) T cells were co-transferred along with irrelevant TCR transgenic CD4⁺ T cells (SMARTA) into CD45.1⁺ congenic recipient mice (Figure 3A). To separate the transferred CD45.2⁺ cells into the correct transgenic populations, we utilized genetically labeled OT-I GFP cells and ex vivo Cell Tracker Blue (CTB)-labeled SMARTA cells. One day later, mice were immunized subcutaneously (s.c) in the flanks with CpG adjuvant and OVA-conjugated fluorescent microspheres to allow for precise tracking of Ag localization in relation to cellular activation. Contralateral dLNs were then harvested at different times postimmunization for comparative histo-cytometry and flow cytometry analyses (Figure 3A).

We used a CD45.2⁺CD45.1[−] binary masking channel to restrict image analysis to the transferred T cells (not shown). We then used the gated CD45.2 signal to generate surfaces for population gating and comparison to flow cytometric data (Figures 3B and 3C). Both methods allowed clear discrimination of CD4⁺GFP⁺ (CD8⁺) events representing OT-I CD8⁺ T cells, of CD4⁺GFP[−]CTB[−] OT-II CD4⁺ T cells, and of CD4⁺GFP[−]CTB⁺ SMARTA CD4⁺ T cells (Figure 3B). The control SMARTA CD4⁺ T cells did not proliferate and did not lose CTB fluorescence over time (Figure S3A and data not shown). Later in the immune response, some of the Ag-specific T cells formed dense cellular aggregates directly around areas with Ag-coated beads (Figure S3B). Certain very tight clusters were difficult to accurately segment into individual objects as noted above and thus were excluded from the quantitative analysis by surface volume gating.

To track the phenotypic changes associated with T cell activation and proliferation, we stained for CD69, an early marker of T cell activation, and Ki-67, which is specifically expressed in the G1-M phases of the cell cycle (Figures 3C and S3B). Both analyses clearly identified expression of CD69, but not Ki-67, early after immunization uniquely on Ag-specific T cell populations (Figures 3C and S3C). Three days after immunization, some of the Ag-specific OT-I and OT-II T cells remained CD69⁺ but a large fraction now showed Ki-67 expression, suggesting that the cells were actively cycling (Figures 3C and 3D, and S3C). Quantitative comparisons of flow and histo-cytometry data sets revealed similar kinetic trends of OT-I and OT-II cellular expansion, as well as of CD69 and Ki-67 expression with respect to the control nondividing SMARTA cells (Figure 3D). Nonetheless, there were some quantitative differences observed with the two methods. By quantifying the increase of Ag-specific T cells in relation to the predominantly stable SMARTA cells (Figure S3A), we found a somewhat reduced expansion of Ag-specific T cells as measured by flow cytometry (Figure 3D).

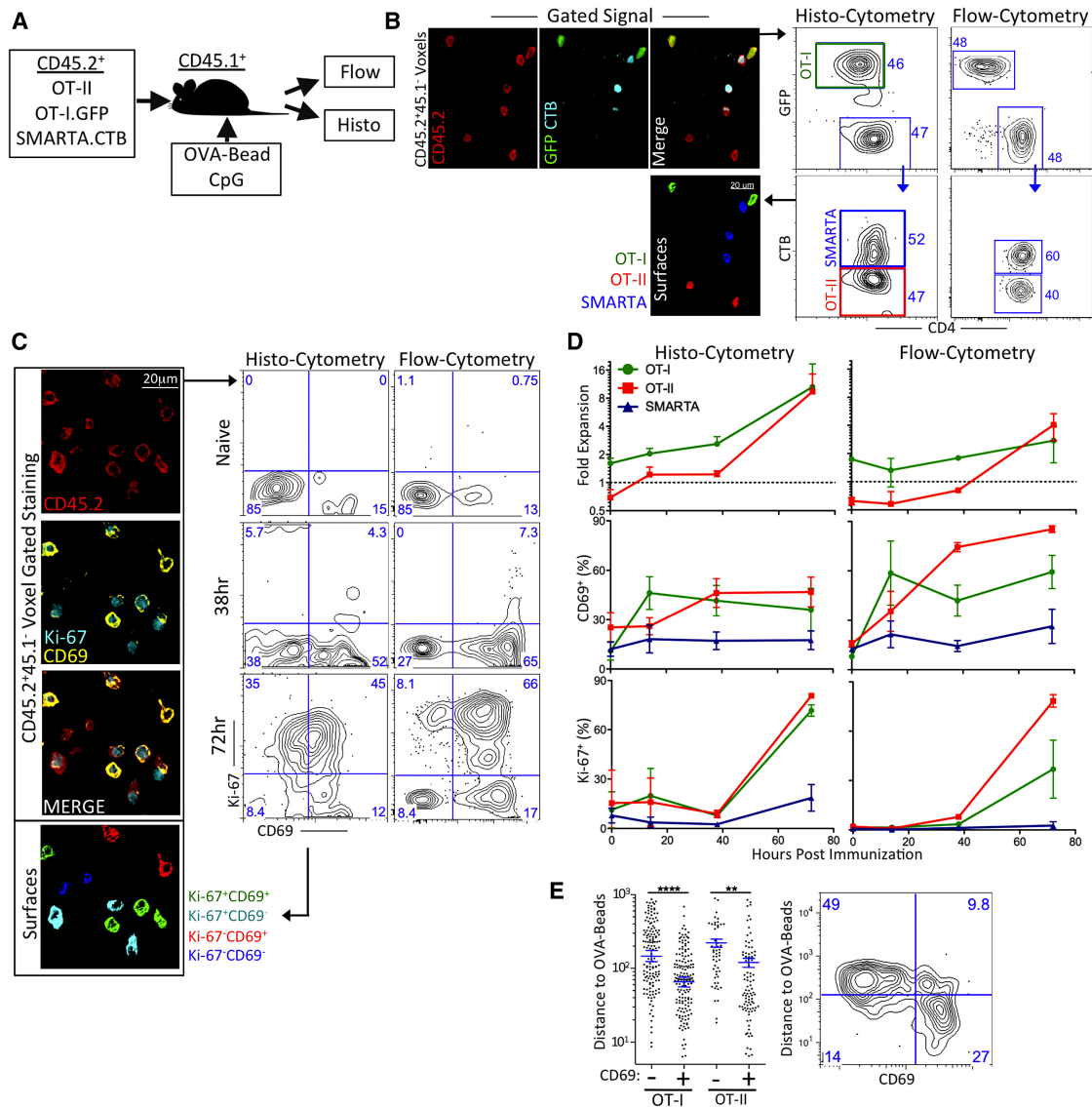


Figure 3. Phenotypic Profiling of T Cell Activation

A total of 1.5×10^6 CD45.2⁺CD44^{low} OT-II, OT-I.GFP and CTB-labeled SMARTA were adoptively transferred into CD45.1⁺ recipients, which were immunized s.c. 1 day later with OVA-conjugated beads and CpG. Contralateral dLN were taken for comparative analysis by flow cytometry and histo-cytometry at indicated time points (A). A CD45.2⁺CD45.1⁺ masking channel was used to gate all other parameters and the gated CD45.2 signal was used to create cell surfaces. CD45.2⁺ surface statistics were plotted for identification of OT-I, OT-II, and SMARTA populations and were visually validated and compared to flow cytometry (B). CD45.2⁺ OT-II surfaces were phenotypically subsetted on the basis of CD69 and Ki-67, visually validated, and compared to flow cytometry (C). The percentage of CD69⁺ and Ki-67⁺ T cell populations, as well as OT-I and -II fold expansion determined by normalization to nondividing SMARTA cells, was quantified (D). Minimum distances of OT-I and -II surfaces to OVA-beads at the 38 hr time point were calculated and compared for the CD69⁺ and CD69⁻ populations (left) and plotted as a 2D contour graph for OT-II (right; E). $n = 3$ for each time point. Error bars represent standard deviation (D) and 95% confidence interval (E).

This potentially reflects poor tissue extraction of highly adhesive, recently activated T cells even with collagenase digestion (Jabbari et al., 2006). Consistent with these findings, we also observed a higher frequency of Ki-67⁺ OT-I CD8⁺ T cells by histo-cytometry (Figure 3D). Finally, there was a reduced frequency of CD69⁺ cells observed by histo-cytometry, likely probably of the lower signal detection and separation for this parameter by microscopic imaging as compared to flow cytometry (Figures 3C and 3D).

To ascertain the spatial distribution of activated T cells in relation to their cognate Ag, we obtained the positional coordinates for T cells and OVA-coated fluorescent microspheres. The latter were clearly visible in dLNs at 14 hr and substantially increased in number at later time points (Figure S3B, not shown). We assumed these Ag-bearing particles were localized in relevant antigen-presenting cell populations within the LN and therefore calculated the closest distances between T cells and microspheres. This analysis revealed a statistically significant

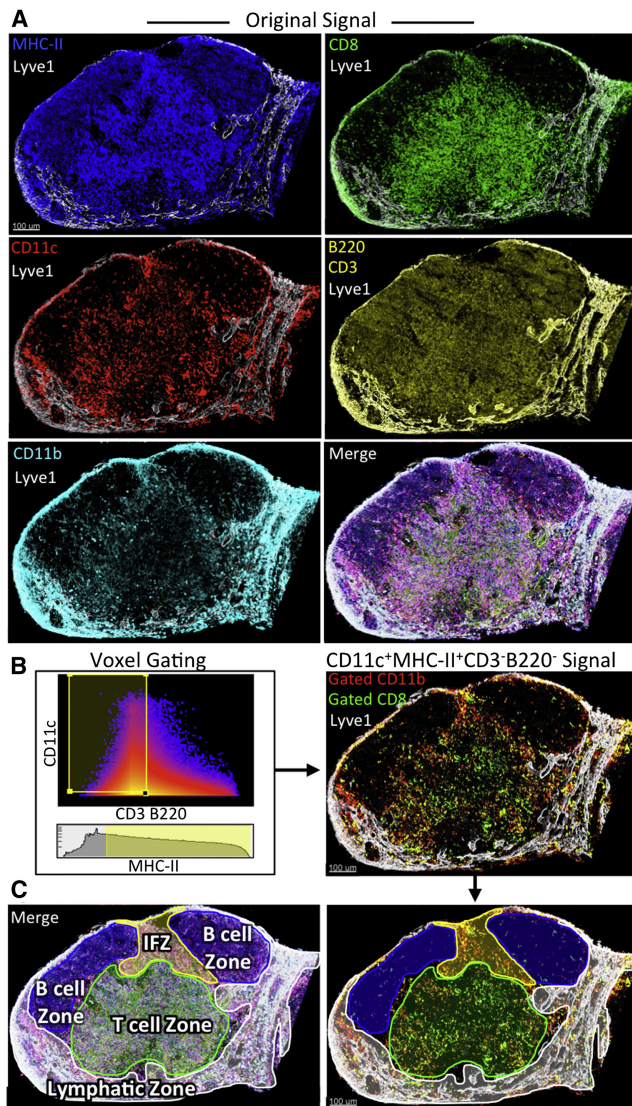


Figure 4. DC Subset Visualization

Inguinal LN sections from C57BL/6 mice were stained with the indicated antibodies and imaged (A). CD11c⁺MHC-II⁺CD3⁻B220⁻ voxel gating allows visualization of CD11b⁺ and CD8⁺ DCs (B). Original (nongated) CD8, CD11c, MHC-II, and Lyve-1 signals provided a clear separation of the LN into discrete zones (C, left): lymphatic, inter-follicular (IFZ), T zone, and B zone, which were overlaid onto the DC-gated CD8 and CD11b image (C, right). A representative of at least three independent imaging sessions is shown.

relationship between CD69⁺ expression and distance from Ag, with the majority of CD69⁺ cells located within 100 μm of the Ag at 38 hr (Figure 3E). This relationship was somewhat underestimated due to cluster (CD69⁺ cells) exclusion and also became less apparent at 72 hr time points, as the number of Ag⁺ cells continued to increase (not shown) and the responding T cells regained motility (Henrickson and von Andrian, 2007). These data demonstrate that histo-cytometry can quantitatively detect cellular phenotypic changes and the spatial positioning of specific activated cell subsets in relationship to distinct points of interest in complex tissues.

DC Subset Visualization

Having tested our method first by identifying basic immune subsets and then cellular phenotypic changes in response to immunization, we applied histo-cytometry to examine the spatial positioning of DC subsets in skin dLN. Inguinal LN sections from C57BL/6 animals were stained with a panel of antibodies to CD11c, MHC-II, CD3, B220, CD8, and CD11b together with antibody to Lyve-1 to mark lymphatic endothelium (Figure 4A). Next, we restricted the image analysis to basic DC subsets by gating on CD8 and CD11b signals within CD11c⁺MHC-II⁺CD3⁻B220⁻ voxels (Figure 4B). The CD8 and CD11b signals largely localized to distinct cells (resident CD8⁺ or resident or migratory CD11b⁺ DCs) that were dispersed throughout the LN paracortex and lymphatic regions with a sparse presence in B cell follicles, as expected. Interestingly, CD8⁺ DCs displayed a more centralized localization in the T cell zone, as compared to more peripherally distributed CD11b⁺ DCs (Figures 4B and 4C). Even though B220⁺CD3⁺ cells were excluded from image analysis, the high density of CD8⁺ T cells in the paracortical T cell zone (Figure 4A) could have introduced elevated amounts of nonspecific CD8 signal into the DC-gated CD8 channel, thus potentially affecting data interpretation. We therefore imaged and analyzed DC subset distribution in LN from *Batf3*^{+/-} and *Batf3*^{-/-} animals (Figure 5A). Because *Batf3*^{-/-} mice are largely devoid of CD8⁺ resident DCs but contain normal numbers of CD8⁺ T cells, any artifacts from misassignment of CD8 signals from T cells to other cell volumes would be evident (Edelson et al., 2010; Hildner et al., 2008). We first restricted image analysis to conventional DC by specifically gating all parameters of interest within CD11c⁺MHC-II⁺CD3⁻B220⁻ voxels. Similar to C57BL/6 mice, *Batf3*^{+/-} LN displayed an abundance of DCs throughout the LN paracortex and not in the B cell follicles, on the basis of the gated CD11c signal (Figure S4B). We observed a clear enrichment of CD8⁺ DCs in the LN center and a denser distribution of CD11b⁺ DCs in the outer cortex and lymphatic regions (Figure 5B). In contrast, *Batf3*^{-/-} animals displayed little to no CD11c⁺MHC-II⁺CD3⁻B220⁻ gated CD8 signal while maintaining a distribution of the gated CD11b signal similar to *Batf3*^{+/-} LNs, thus validating the observed CD8⁺ DC distribution in wild-type animal LNs (Figure 5B).

We then created DC surfaces, on the basis of the gated CD11c signal, and analyzed DC populations via contour plot analysis and direct comparison to flow cytometry data. Both analyses allowed discrimination of CD11c^{hi}MHC-II^{int} resident and CD11c^{int}MHC-II^{hi} migratory DC populations (Figure 5C), albeit the resolution of subpopulations by flow cytometry was noticeably clearer than that achieved with histo-cytometry for the reasons noted above. The threshold cutoffs for the gating were validated by examining CD11c and MHC-II expression on migratory CD207⁺ DCs (Figure S4A). Resident DC analysis revealed distinct CD11b⁺ and CD8⁺ subset separation by both analytical methods, with the CD8⁺ sub-population being clearly absent in the *Batf3*^{-/-} animals (Figure 5C). Moreover, we observed highly comparable quantification of resident DC subset composition via flow and histo-cytometry, with *Batf3*^{-/-} animals having reduced percentages of CD8⁺ DCs and increased percentages of CD11b⁺ DCs (Figure 5D). Importantly, histo-cytometry allowed us to quantitatively examine subset-specific localization differences (Figures 5C and 5E). Analysis based on

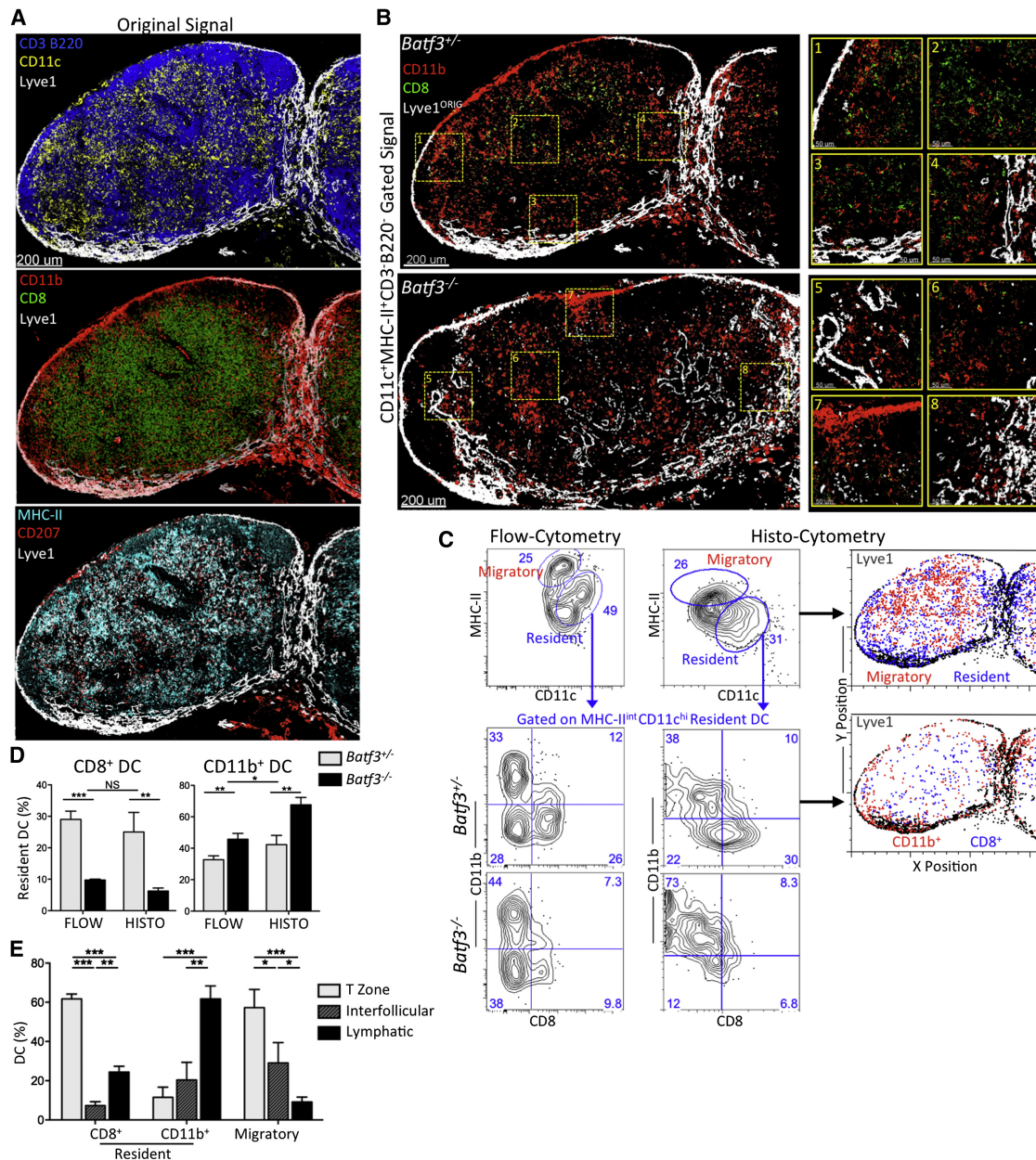


Figure 5. Resident DC Subset Visualization and Quantification

Inguinal *Batf3*^{+/-} and *Batf3*^{-/-} LN sections were stained with the indicated antibodies and imaged (A, *Batf3*^{+/-} presented). CD11c⁺MHC-II⁺CD3⁻B220⁻ voxel gated CD11b and CD8 signals are displayed for *Batf3*^{+/-} and *Batf3*^{-/-} LN sections (B). DC surface statistics were used for identification and spatial visualization of resident CD8⁺ and CD11b⁺ DC subsets, with confirmation by flow cytometry for CD3⁻NK1.1⁻CD19⁻CD11c⁺MHC⁺ gated DC subsets (C). Frequencies of CD11c^{hi}MHC-II^{int} resident CD8⁺ and CD11b⁺ DCs were quantified and compared to results obtained by flow cytometry (D). The percentage of cells localized to the indicated zones within the indicated DC subsets was quantified (E). A representative of at least two independent experiments is shown; n = 3. Error bars represent the SD.

predefined subregions in the LNs (Figure S4B) showed predominant localization of resident CD8⁺ DCs to the T cell zone, albeit some cells with this phenotype were also present in other regions, and the principal localization of resident CD11b⁺ DC to the lymphatic regions with a relatively minor presence of these DC elsewhere (Figures 5E and S4B). These differences were reproduced in normal B6 mice (Figure 4 and data not shown), in CD11c-YFP reporter mice for inguinal, popliteal, and auricular

LNs (Figures S4C–S4E), and in additional experiments that employed CD205 (instead of CD8) for identifying CD8⁺ resident DCs (Figure S4F). Minor morphological oversegmentation artifacts did not affect the regionalized distribution of DC subsets derived from this analysis (data not shown).

Interestingly, migratory DCs showed a mixed distribution between the interfollicular and T cell zones and were largely absent from the medullary region (Figure 5F), consistent with

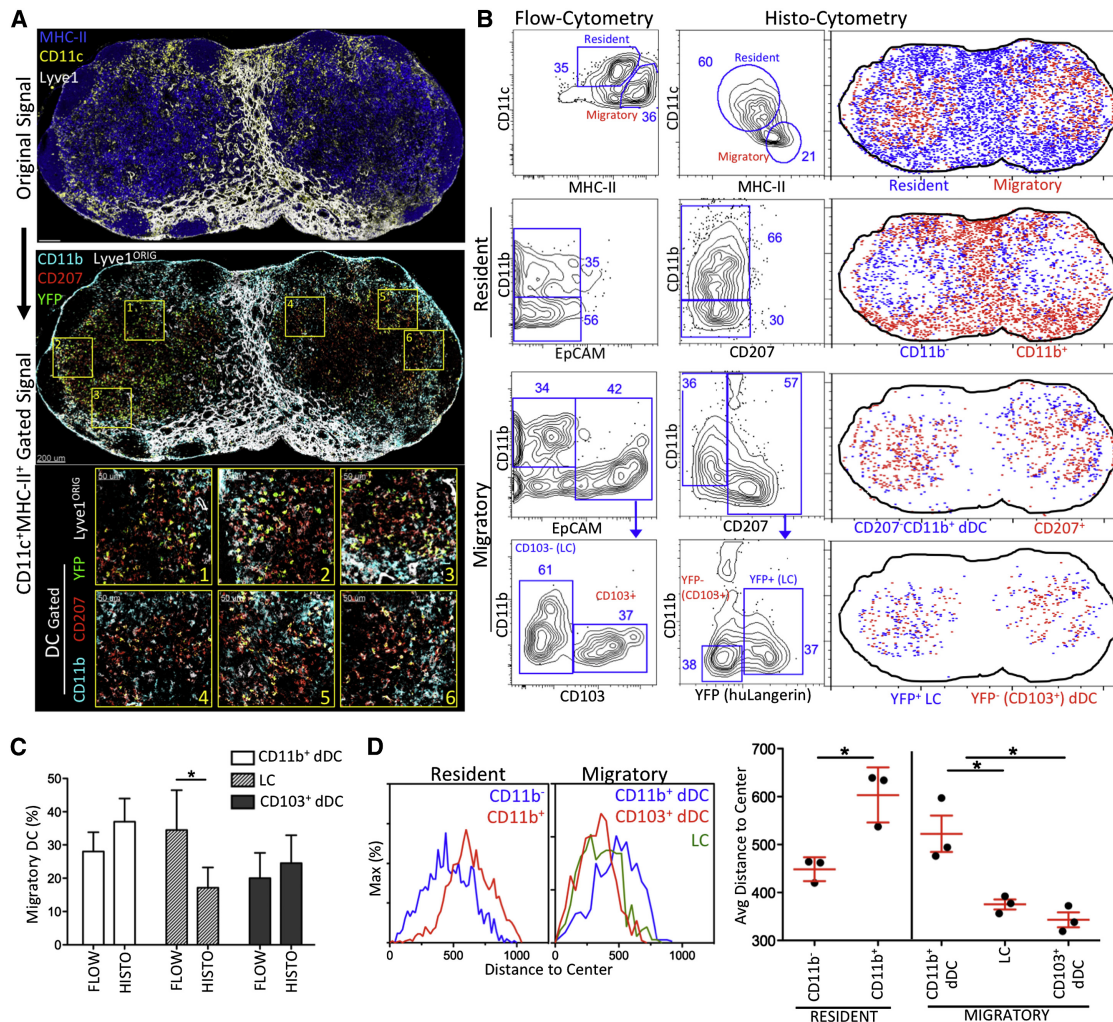


Figure 6. Migratory DC Subset Visualization

Inguinal LN sections from (human-promoter)Langerin-Cre × YFP-flox reporter animals were stained with the indicated antibodies and imaged (A). Resident and migratory DC subsets were identified and spatially visualized by histo-cytometry (LN outline added for clarity), with confirmation by flow cytometric evaluation of CD3⁺NK1.1⁺CD19⁺CD11c⁺MHC⁺ gated DC subsets (B). Migratory DC subset compositions derived by both analytical methods were quantitatively compared (C). Distance to the LN lobe center for individual cells of distinct DC subsets were compared (D, left), and the average distance for the different populations in three individual LNs was quantified (D, right). *n* = 3. Error bars represent the SD.

the recent observations of localized DC immigration into the LN parenchyma through the interfollicular regions (Braun et al., 2011; Schumann et al., 2010). To further assess localization of migratory DC subsets, we attempted to costain LN sections with CD11b, CD207, and CD103. Unfortunately, neither the 2E7 or M290 CD103 antibody clones nor a polyclonal antibody to this marker yielded reproducible and specific staining consistent with the CD207 signal distribution (data not shown). Instead, we turned to a recently described langerin (CD207) YFP reporter driven by the human and not the mouse langerin promoter, in which only the CD207⁺ LCs and not the CD103⁺CD207⁺ dermal DCs (dDCs) express the YFP protein (Hattori et al., 2011; Kaplan, 2010; Kaplan et al., 2007). Staining of LN sections from these animals with the CD207 antibody was expected to reveal two populations of cells: CD207⁺YFP⁺ LCs and CD207⁺YFP⁺CD103⁺ dDCs. Consistent with this prediction, analysis of

CD11c⁺MHC-II⁺ gated CD11b, CD207, and YFP channels revealed a highly variegated distribution of CD11b signal, with dense staining in the lymphatic zone (largely resident CD11b⁺ DCs) and in the interfollicular zone (presumably migratory CD11b⁺ dDCs), and distinct localization of CD207⁺YFP⁺ and CD207⁺YFP⁺ signals mainly deep in the T cell zone (Figure 6A). Volumetric DC rendering and histo-cytometry analysis of CD11c^{int}MHC-II^{hi} migratory DC revealed a clear-cut separation of CD11b⁺CD207⁺ dDC, CD207⁺YFP⁺ LC, and CD207⁺YFP⁺ dDC populations (Figure 6B). As expected, CD207 was absent from the resident DC populations. Flow cytometric evaluation of these populations (with EpCAM used instead of CD207 for the analysis) revealed a highly similar migratory DC subset composition and quantitative result (Figures 6B and 6C). Importantly, histo-cytometry allowed us to analyze subset-specific localization differences. Consistent with the data presented

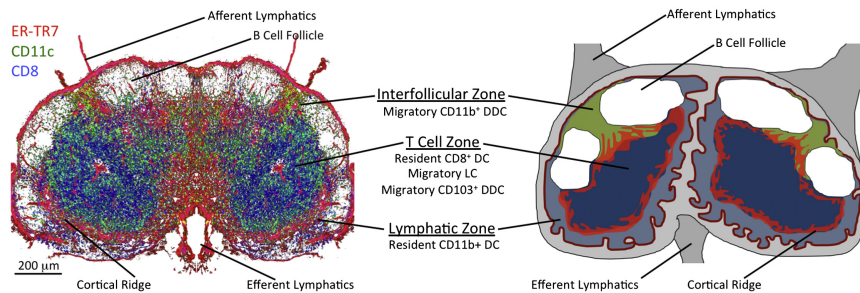


Figure 7. Microanatomical Separation of Distinct DC Subsets

Immunofluorescence microscopy-based (left) and cartoon (right) models of the predominant distribution of different resident and migratory DC subsets among discrete LN microcompartments are presented (see text). Staining for the stromal marker ER-TR7 allows for direct visualization of LN compartmentalization into discrete microdomains, with clear T cell zone demarcation (indicated by the CD8 stain) from the interfollicular and lymphatic regions (left). The microscopy image was mirrored and the afferent lymphatic vessels added for enhanced model clarity.

above, the resident $CD11b^-$ and $CD11b^+$ DCs differentially distributed between the T cell zone and the lymphatic regions, respectively, as analyzed by the distance to LN lobe center (Figures 6B and 6D). Interestingly, the migratory DC subsets also were differentially distributed, with the $CD11b^+$ dDCs located far away from the LN center, in or near the interfollicular zones (peripheral paracortex). On the other hand, we did not observe major localization differences between the $CD103^+$ dDCs and the LCs, with the large majority of both cell types located deep inside the LN paracortex (Figures 6B and 6D). The spatial distribution differences between the $CD11b^+$ dDC and $CD207^+$ migratory DC populations were observed in non-transgenic animals, in $CD11c$ -YFP reporter mice, and after chemical-induced skin irritation, although the regionalized localization was somewhat less pronounced in this case (Figure S5). Together, these data demonstrate a previously unappreciated diverse microanatomical positioning of distinct resident and migratory DC subsets in steady state LNs (Figure 7).

DISCUSSION

Determining both individual cellular identity and precise spatial distribution of multiple populations within complex organs is a long-standing goal in many fields of biology. However, it can be highly problematic to clearly identify and visualize populations defined by several nonexclusive markers in highly heterogeneous and densely packed biological tissues. Histo-cytometry permits analytical processing of stained tissue section images for visualization and quantitative gating of cellular subsets and phenotypes defined by dense multiparametric marker combinations. This technique was validated in large cross-sections of mouse LNs by identifying and analyzing the distribution of various leukocytes. We were able to spatially separate basic immune populations, including $CD4^+$ and $CD8^+$ T cells, B cells and DCs, to visualize the early stages of Ag-specific T cell activation and proliferation with respect to the localization of cognate Ag, and to decipher the intranodal spatial anatomy of all major conventional DC subsets. For well-isolated cells, histo-cytometry achieved cell phenotyping and enumeration results quantitatively similar to flow cytometry, the “gold standard” for cell identification and enumeration, while surpassing flow results with respect to cells that are difficult to extract from tissue.

Several commercial platforms have been specifically designed for identification and phenotypic analysis of cells directly in tissue sections (Ecker and Steiner, 2004; Harnett, 2007).

However, these systems typically require specialized microscope systems and software and do not allow for spillover correction, deconvolution, and voxel gating. Some of these existing approaches choose to limit axial resolution in an attempt to maximize signal collection and are restricted to 2D cellular analysis, thus not permitting accurate volumetric image interrogation of complex tissues and multiple diverse cell types. An alternative approach to simultaneous multiplexed antibody labeling, called multi-epitope-ligand cartography (MELC), has been demonstrated to allow robust sampling of hundreds of different antibody probes labeled with the same fluorophore by utilizing sequential staining, imaging, and fluorophore bleaching (Schubert et al., 2006). Although being a powerful method for “toponome” mapping, MELC is limited by the need for special robotic instrumentation, very long imaging runs, and binary signal compression (Schubert et al., 2006). Histo-cytometry, on the other hand, is an analytical pipeline that utilizes widely available microscope equipment and image analysis platforms along with commonly available fluorophores and combinations of antibodies already in use for conventional flow cytometry and thus can be rapidly integrated into current laboratory workflows.

Our findings obtained with histo-cytometry substantially extend previous studies that suggested a nonrandom distribution of some DC subsets within lymphoid tissues. We visualized and quantified nearly all well-defined LN DC subsets in tissue sections on the basis of classical marker definitions established by flow cytometry, revealing a clear regionalization of DC populations to discrete anatomical subcompartments in murine LNs. It is important to note that each of the delimited LN regions was not occupied exclusively by one DC subset and any given subset did not reside exclusively in one region; rather, the indicated subsets showed heavily skewed distributions with predominance in the indicated locations. Most previous studies addressing this issue have described the localized distribution of a limited number of distinct resident DCs in the spleen. Such an analysis has been challenging to achieve in LNs, where multiple migratory and resident subsets with overlapping markers are present (Dudziak et al., 2007; Qiu et al., 2009).

Resident $CD8^+$ and $CD11b^+$ DC subsets largely segregated to the T cell zone or the lymphatic zone of the LN, respectively. This is highly reminiscent of differential localization of splenic $CD205^+$ ($CD8^+$) and $33D1^+$ ($CD11b^+$) resident DCs to the T cell zone and the red pulp (respectively), the spatial separation of $CD205$ and $CD11b$ signal observed in the LN, and the localization of

Necln-like protein 2⁺ cells (CD8⁺ DCs) to the T cell zones in human and murine spleens (Dudziak et al., 2007; Galibert et al., 2005; Sixt et al., 2005). Migratory DC subsets also segregated into distinct anatomical zones, with the CD11b⁺ dDCs largely inhabiting interfollicular and outer paracortical regions and with the LCs and CD103⁺ dDCs accumulating deeper in the T cell zones. These latter findings are similar to those previously reported in a skin irritation and fluorophore painting model (Kissenpfennig et al., 2005), with the addition that we were able to achieve specific localization of all currently known migratory DC subsets, including the resolution of the CD207⁺ CD103⁺ dDCs from the LCs. In addition, histo-cytometry permitted observation of migratory DC localization in LNs not only in inflammatory settings but in the steady state.

These observations suggest that different DC subsets preferentially respond to spatially distinct cues, which may include ligands for chemokine receptors, integrins, and/or lectins that guide them to specialized locations within lymphoid tissues. It is likely that stromal cells contribute to this regionalization of DC subsets by providing population-specific cues. Differential stromal cell compositions and structures in LNs have been previously described (Katakai et al., 2004; Mueller and Germain, 2009). Overall, these results point to a highly complex and regulated LN organization, with DC subsets segregation creating compartments with distinct properties with respect to Ag access and MHC presentation, TLR-induced maturation, and inflammatory cytokine production. In turn, this may lead to regional specialization for T cell activation and effector differentiation. In accord with this notion, preliminary studies in our laboratory have revealed differential Ag uptake by DC subsets that match predictions based on these newly described spatial distributions. These studies also show specialized zones of initial CD8⁺ and CD4⁺ T cell migration arrest and activation that both fit with these location-associated antigen acquisition data and previously described DC subset specialization in MHC-I and MHC-II processing machinery (unpublished data; Heath and Carbone, 2009; Shortman and Heath, 2010).

Both flow cytometry and histo-cytometry have specific limitations and advantages, with flow cytometry excelling at high throughput analysis of single-cell suspensions of readily extractable cells and histo-cytometry able to visualize and quantify cellular subsets directly within tissues. These techniques are thus best applied as complimentary approaches. Importantly, histo-cytometry can be directly applied to highly precious nonhuman primate and human samples that cannot be subjected to transgenic reporter-based or large-scale flow cytometric analyses, and we have recently successfully applied elements of histo-cytometry to the in situ detection and spatial characterization of T follicular helper cells in SIV-infected rhesus macaques (Petrovas et al., 2012). This technique can also be employed to collect additional types of information (e.g., localization of specific phospho-proteins and cytokines in tissues). We thus believe that histo-cytometry offers the ability to investigate the relationships between cellular subsets and their anatomical distribution, location-based function, differentiation and activation state, and intercellular interactions across different biological systems of interest and in different species.

EXPERIMENTAL PROCEDURES

Mice

CD45.1⁺ C57BL/6, CD11c-YFP (Lindquist et al., 2004) and C57BL/6 OT-II TCR transgenic mice (Barnden et al., 1998) were obtained from Taconic Laboratories. OT-I CD8⁺ T cell transgenic mice (Hogquist et al., 1994) were obtained from Taconic and crossed to C57BL/6 ubiquitin-GFP mice (Schaefer et al., 2001) (Jackson Laboratories). SMARTA CD4⁺ T cell transgenic animals (Oxenius et al., 1998) were provided by E. Shevach (National Institutes of Health, Bethesda, MD, USA). *Batf3*^{-/-} mice on the 129 background (Hildner et al., 2008) were provided by K. Murphy (University of Washington, St. Louis, MI, USA) and backcrossed to C57BL/6 for two generations. *Batf3*^{+/-} littermates were used as controls. LNs from (human-promoter)Langerin-Cre × YFP-flox mice were provided by D.H. Kaplan (Hattori et al., 2011; Kaplan et al., 2007). All mice were maintained in specific-pathogen-free conditions at an Association for Assessment and Accreditation of Laboratory Animal Care-accredited animal facility at the NIAID. All procedures were approved by the NIAID Animal Care and Use Committee (National Institutes of Health, Bethesda, MD, USA).

Microscopy and Histo-Cytometry

Detailed methods for sample preparation, imaging, and data processing are available in the Supplemental Experimental Procedures.

BM Chimeras, Adoptive Transfers, and Immunization

CD45.1⁺CD45.2⁻ animals were exposed twice to 600 rad of gamma irradiation from a cesium source separated by a 3 hr rest period. A total of 5×10^6 total donor BM cells, spiked with 1%, 5%, or 10% of CD45.2⁺CD45.1⁻ cells, were injected intravenously (i.v.) the same day. Mice were rested and given Neomycin or Sulfatrim water afterward for 4 weeks. Tissues from chimeric animals were harvested for flow cytometry and histo-cytometry analyses 6 weeks after irradiation.

Naive (CD44^{low}) OT-I, OT-II, and SMARTA T cells were purified from LN and spleen tissues by Miltenyi negative selection T cell isolation kits (Miltenyi Biotec) in combination with 1:10,000 CD44-bio antibody. SMARTA T cells were labeled with CMF2HC (4-chloromethyl-6,8-difluoro-7-hydroxycoumarin) CTB at 100 μM concentration and 1:10 pluronic polyol:dye ratio (Invitrogen) for 15 min at 37°C and washed with 10% fetal calf serum RPMI media. A total of 1.5×10^6 CD45.2⁺ OT-I.GFP, OT-II, and CTB-labeled SMARTA cells were adoptively transferred i.v. into CD45.1⁺ recipient mice. One day later, animals were immunized with 25 μg of CpG 1668 and $\sim 10^6$ to 10^7 blue-green fluorescent FluoSpheres polystyrene microspheres (Invitrogen) covalently conjugated with OVA protein (Sigma-Aldrich). Inguinal dLNs were harvested at various times after immunization. In some animals, ear pinnae were irritated by skin application of 10 μl of 50:50 (V:V) of dibutyl phthalate:acetone, with dLNs harvested 3 days later.

Cell Isolation and Flow Cytometry

Inguinal LNs were harvested and treated with 400 U/ml collagenase D (Roche Applied Science) solution for 25 min at 37°C. EDTA (10 mM) was added for 1 min and quenched with PBS wash. Single-cell suspensions were stained with the indicated antibodies, acquired on a LSR-II flow cytometer (BD Biosciences), and analyzed with FlowJo software (TreeStar).

Statistical Analysis

The statistical significance of differences in mean values was analyzed by a two-tailed Student's t test. ***p < 0.0001, **p < 0.005, and *p < 0.05.

SUPPLEMENTAL INFORMATION

Supplemental Information includes Supplemental Experimental Procedures and five figures and can be found with this article online at <http://dx.doi.org/10.1016/j.immuni.2012.07.011>.

ACKNOWLEDGMENTS

Several individuals contributed to the development of this work. O.M. Schwartz and S. Becker provided training and expertise for confocal imaging.

M. Roederer provided essential expertise in spillover correction and data transformation for FlowJo-based analysis. D.H. Kaplan and B.Z. Igyarto provided the (human-promoter)Langerin-Cre x eYFP-flox mice and advice in migratory DC visualization. J. Schenkel provided advice with antibody clone selection. T. Laemmerman and K.A. Casey provided critical manuscript reviews and general project advice. This work was supported by the Intramural Research Program of NIAID, NIH.

Received: March 23, 2012

Revised: June 26, 2012

Accepted: July 17, 2012

Published online: August 2, 2012

REFERENCES

- Ansel, K.M., McHeyzer-Williams, L.J., Ngo, V.N., McHeyzer-Williams, M.G., and Cyster, J.G. (1999). In vivo-activated CD4 T cells upregulate CXC chemokine receptor 5 and reprogram their response to lymphoid chemokines. *J. Exp. Med.* 190, 1123–1134.
- Barnden, M.J., Allison, J., Heath, W.R., and Carbone, F.R. (1998). Defective TCR expression in transgenic mice constructed using cDNA-based alpha- and beta-chain genes under the control of heterologous regulatory elements. *Immunol. Cell Biol.* 76, 34–40.
- Bendall, S.C., Simonds, E.F., Qiu, P., Amir, A.D., Krutzik, P.O., Finck, R., Bruggner, R.V., Melamed, R., Trejo, A., Ornatsky, O.I., et al. (2011). Single-cell mass cytometry of differential immune and drug responses across a human hematopoietic continuum. *Science* 332, 687–696.
- Braun, A., Worbs, T., Moschovakis, G.L., Halle, S., Hoffmann, K., Bölter, J., Münk, A., and Förster, R. (2011). Afferent lymph-derived T cells and DCs use different chemokine receptor CCR7-dependent routes for entry into the lymph node and intranodal migration. *Nat. Immunol.* 12, 879–887.
- Chow, A., Brown, B.D., and Merad, M. (2011). Studying the mononuclear phagocyte system in the molecular age. *Nat. Rev. Immunol.* 11, 788–798.
- Conchello, J.A., and Lichtman, J.W. (2005). Optical sectioning microscopy. *Nat. Methods* 2, 920–931.
- Dudzziak, D., Kamphorst, A.O., Heidkamp, G.F., Buchholz, V.R., Trumpfheller, C., Yamazaki, S., Cheong, C., Liu, K., Lee, H.W., Park, C.G., et al. (2007). Differential antigen processing by dendritic cell subsets in vivo. *Science* 315, 107–111.
- Ecker, R.C., and Steiner, G.E. (2004). Microscopy-based multicolor tissue cytometry at the single-cell level. *Cytometry A* 59, 182–190.
- Edelson, B.T., Bradstreet, T.R., Hildner, K., Carrero, J.A., Frederick, K.E., Kc, W., Belizaire, R., Aoshi, T., Schreiber, R.D., Miller, M.J., et al. (2011). CD8 α (+) dendritic cells are an obligate cellular entry point for productive infection by *Listeria monocytogenes*. *Immunity* 35, 236–248.
- Edelson, B.T., Kc, W., Juang, R., Kohyama, M., Benoit, L.A., Klekotka, P.A., Moon, C., Albring, J.C., Ise, W., Michael, D.G., et al. (2010). Peripheral CD103+ dendritic cells form a unified subset developmentally related to CD8 α conventional dendritic cells. *J. Exp. Med.* 207, 823–836.
- Edwards, A.D., Diebold, S.S., Slack, E.M., Tomizawa, H., Hemmi, H., Kaisho, T., Akira, S., and Reis e Sousa, C. (2003). Toll-like receptor expression in murine DC subsets: lack of TLR7 expression by CD8 α + DC correlates with unresponsiveness to imidazoquinolines. *Eur. J. Immunol.* 33, 827–833.
- Galibert, L., Diemer, G.S., Liu, Z., Johnson, R.S., Smith, J.L., Walzer, T., Comeau, M.R., Rauch, C.T., Wolfson, M.F., Sorensen, R.A., et al. (2005). Nectin-like protein 2 defines a subset of T-cell zone dendritic cells and is a ligand for class-I-restricted T-cell-associated molecule. *J. Biol. Chem.* 280, 21955–21964.
- Garini, Y., Young, I.T., and McNamara, G. (2006). Spectral imaging: principles and applications. *Cytometry A* 69, 735–747.
- Garside, P., Ingulli, E., Merica, R.R., Johnson, J.G., Noelle, R.J., and Jenkins, M.K. (1998). Visualization of specific B and T lymphocyte interactions in the lymph node. *Science* 281, 96–99.
- Germain, R.N. (2004). An innately interesting decade of research in immunology. *Nat. Med.* 10, 1307–1320.
- Harnett, M.M. (2007). Laser scanning cytometry: understanding the immune system in situ. *Nat. Rev. Immunol.* 7, 897–904.
- Hattori, T., Chauhan, S.K., Lee, H., Ueno, H., Dana, R., Kaplan, D.H., and Saban, D.R. (2011). Characterization of Langerin-expressing dendritic cell subsets in the normal cornea. *Invest. Ophthalmol. Vis. Sci.* 52, 4598–4604.
- Heath, W.R., and Carbone, F.R. (2009). Dendritic cell subsets in primary and secondary T cell responses at body surfaces. *Nat. Immunol.* 10, 1237–1244.
- Helft, J., Ginhoux, F., Bogunovic, M., and Merad, M. (2010). Origin and functional heterogeneity of non-lymphoid tissue dendritic cells in mice. *Immunol. Rev.* 234, 55–75.
- Hell, S.W. (2009). Microscopy and its focal switch. *Nat. Methods* 6, 24–32.
- Henrickson, S.E., and von Andrian, U.H. (2007). Single-cell dynamics of T-cell priming. *Curr. Opin. Immunol.* 19, 249–258.
- Hildner, K., Edelson, B.T., Purtha, W.E., Diamond, M., Matsushita, H., Kohyama, M., Calderon, B., Schraml, B.U., Unanue, E.R., Diamond, M.S., et al. (2008). Batf3 deficiency reveals a critical role for CD8 α + dendritic cells in cytotoxic T cell immunity. *Science* 322, 1097–1100.
- Hogquist, K.A., Jameson, S.C., Heath, W.R., Howard, J.L., Bevan, M.J., and Carbone, F.R. (1994). T cell receptor antagonist peptides induce positive selection. *Cell* 76, 17–27.
- Itoyaga, J., Suda, N., Suda, K., Park, C.G., and Steinman, R.M. (2009). Antibody to Langerin/CD207 localizes large numbers of CD8 α + dendritic cells to the marginal zone of mouse spleen. *Proc. Natl. Acad. Sci. USA* 106, 1524–1529.
- Igyártó, B.Z., Haley, K., Ortner, D., Bobr, A., Gerami-Nejad, M., Edelson, B.T., Zurawski, S.M., Malissen, B., Zurawski, G., Berman, J., and Kaplan, D.H. (2011). Skin-resident murine dendritic cell subsets promote distinct and opposing antigen-specific T helper cell responses. *Immunity* 35, 260–272.
- Jabbari, A., Legge, K.L., and Harty, J.T. (2006). T cell conditioning explains early disappearance of the memory CD8 T cell response to infection. *J. Immunol.* 177, 3012–3018.
- Kaplan, D.H. (2010). In vivo function of Langerhans cells and dermal dendritic cells. *Trends Immunol.* 31, 446–451.
- Kaplan, D.H., Li, M.O., Jenison, M.C., Shlomchik, W.D., Flavell, R.A., and Shlomchik, M.J. (2007). Autocrine/paracrine TGF β 1 is required for the development of epidermal Langerhans cells. *J. Exp. Med.* 204, 2545–2552.
- Kastenmuller, W., Torabi-Parizi, P., Subramanian, S., Lammermann, T., and Germain, R.N. (2012). A spatially-organized multicellular innate immune response in the lymph node limits the systemic spread of tissue-invasive pathogens. *Cell* 151. <http://dx.doi.org/10.1016/j.cell.2012.07.021>.
- Katakai, T., Hara, T., Lee, J.H., Gonda, H., Sugai, M., and Shimizu, A. (2004). A novel reticular stromal structure in lymph node cortex: an immuno-platform for interactions among dendritic cells, T cells and B cells. *Int. Immunol.* 16, 1133–1142.
- Kissenpfennig, A., Henri, S., Dubois, B., Laplace-Builhé, C., Perrin, P., Romani, N., Tripp, C.H., Douillard, P., Leserman, L., Kaiserlian, D., et al. (2005). Dynamics and function of Langerhans cells in vivo: dermal dendritic cells colonize lymph node areas distinct from slower migrating Langerhans cells. *Immunity* 22, 643–654.
- Köhler, G., and Milstein, C. (1975). Continuous cultures of fused cells secreting antibody of predefined specificity. *Nature* 256, 495–497.
- Lindquist, R.L., Shakhar, G., Dudziak, D., Wardemann, H., Eisenreich, T., Dustin, M.L., and Nussenzweig, M.C. (2004). Visualizing dendritic cell networks in vivo. *Nat. Immunol.* 5, 1243–1250.
- Mueller, S.N., and Germain, R.N. (2009). Stromal cell contributions to the homeostasis and functionality of the immune system. *Nat. Rev. Immunol.* 9, 618–629.
- Newell, E.W., Sigal, N., Bendall, S.C., Nolan, G.P., and Davis, M.M. (2012). Cytometry by time-of-flight shows combinatorial cytokine expression and virus-specific cell niches within a continuum of CD8+ T cell phenotypes. *Immunity* 36, 142–152.
- Oxenius, A., Bachmann, M.F., Zinkernagel, R.M., and Hengartner, H. (1998). Virus-specific MHC-class II-restricted TCR-transgenic mice: effects on

- humoral and cellular immune responses after viral infection. *Eur. J. Immunol.* 28, 390–400.
- Perfetto, S.P., Chattopadhyay, P.K., and Roederer, M. (2004). Seventeen-colour flow cytometry: unravelling the immune system. *Nat. Rev. Immunol.* 4, 648–655.
- Petrovas, C., Yamamoto, T., Gerner, M.Y., Boswell, K.L., Wloka, K., Smith, E.C., Ambrozak, D.R., Sandler, N.G., Timmer, K.J., Sun, X., et al. (2012). Follicular helper CD4⁺ T cell dynamics during SIV infection. *J. Clin. Invest.* Published online August 27, 2012.
- Qiu, C.H., Miyake, Y., Kaise, H., Kitamura, H., Ohara, O., and Tanaka, M. (2009). Novel subset of CD8α⁺ dendritic cells localized in the marginal zone is responsible for tolerance to cell-associated antigens. *J. Immunol.* 182, 4127–4136.
- Reif, K., Ekland, E.H., Ohl, L., Nakano, H., Lipp, M., Förster, R., and Cyster, J.G. (2002). Balanced responsiveness to chemoattractants from adjacent zones determines B-cell position. *Nature* 416, 94–99.
- Roederer, M. (2002). Compensation in flow cytometry. *Curr. Protoc. Cytom. Chapter 1*, 1–, 14.
- Rothfuchs, A.G., Egen, J.G., Feng, C.G., Antonelli, L.R., Bafica, A., Winter, N., Locksley, R.M., and Sher, A. (2009). In situ IL-12/23p40 production during mycobacterial infection is sustained by CD11b^{high} dendritic cells localized in tissue sites distinct from those harboring bacilli. *J. Immunol.* 182, 6915–6925.
- Sancho, D., Joffre, O.P., Keller, A.M., Rogers, N.C., Martínez, D., Hernanz-Falcón, P., Rosewell, I., and Reis e Sousa, C. (2009). Identification of a dendritic cell receptor that couples sensing of necrosis to immunity. *Nature* 458, 899–903.
- Schaefer, B.C., Schaefer, M.L., Kappler, J.W., Marrack, P., and Kiedl, R.M. (2001). Observation of antigen-dependent CD8⁺ T-cell/ dendritic cell interactions in vivo. *Cell. Immunol.* 214, 110–122.
- Schubert, W., Bonnekoh, B., Pommer, A.J., Philipsen, L., Böckelmann, R., Malykh, Y., Gollnick, H., Friedenberger, M., Bode, M., and Dress, A.W. (2006). Analyzing proteome topology and function by automated multidimensional fluorescence microscopy. *Nat. Biotechnol.* 24, 1270–1278.
- Schumann, K., Lämmermann, T., Brückner, M., Legler, D.F., Polleux, J., Spatz, J.P., Schuler, G., Förster, R., Lutz, M.B., Sorokin, L., and Sixt, M. (2010). Immobilized chemokine fields and soluble chemokine gradients cooperatively shape migration patterns of dendritic cells. *Immunity* 32, 703–713.
- Scriven, D.R., Lynch, R.M., and Moore, E.D. (2008). Image acquisition for colocalization using optical microscopy. *Am. J. Physiol. Cell Physiol.* 294, C1119–C1122.
- Shortman, K., and Heath, W.R. (2010). The CD8⁺ dendritic cell subset. *Immunol. Rev.* 234, 18–31.
- Sixt, M., Kanazawa, N., Selg, M., Samson, T., Roos, G., Reinhardt, D.P., Pabst, R., Lutz, M.B., and Sorokin, L. (2005). The conduit system transports soluble antigens from the afferent lymph to resident dendritic cells in the T cell area of the lymph node. *Immunity* 22, 19–29.
- Smith-Garvin, J.E., Koretzky, G.A., and Jordan, M.S. (2009). T cell activation. *Annu. Rev. Immunol.* 27, 591–619.
- Villadangos, J.A., and Schnorrer, P. (2007). Intrinsic and cooperative antigen-presenting functions of dendritic-cell subsets in vivo. *Nat. Rev. Immunol.* 7, 543–555.
- Vremec, D., Zorbas, M., Scollay, R., Saunders, D.J., Ardavin, C.F., Wu, L., and Shortman, K. (1992). The surface phenotype of dendritic cells purified from mouse thymus and spleen: investigation of the CD8 expression by a subpopulation of dendritic cells. *J. Exp. Med.* 176, 47–58.